

## Grazing-Incidence Small-Angle Scattering (GISAXS)

Detlef-M. Smilgies, Cornell High Energy Synchrotron Source (CHESS)

Contributed article to “The SAXS Guide”, 4<sup>th</sup> edition, published by Anton Paar Company (2017).

### Introduction

GISAXS has developed into an important tool to study nanostructured surfaces and thin films [1]. Soft materials have been of particular interest, as many of them can be solution processed and self-organize on a nanometer length scale. Well-known examples are conjugated polymers and molecules for organic electronics (typical d-spacings from 1 nm to 10 nm), lipids (3-30 nm), nanoparticles (3-30 nm), as well as block copolymers (10-100 nm). Such systems are of interest to use with industrial coating and printing techniques for flexible consumer electronics, medical sensors, and many other applications.

Now, why do we need grazing incidence for this purpose? X-rays have peculiar optical properties. In particular, their complex refractive index  $n$  is slightly less than one:

$$n = 1 - \delta + i\beta$$

where  $\delta$  is the dispersive part governing refraction, and  $\beta$  accounts for absorption.  $\delta$  is on the order of  $10^{-6}$ - $10^{-5}$  for common elements. This property has important consequences, when we apply Snell's law: x-rays feature total *external* refraction, i.e. total reflection occurs on the air or vacuum side, as opposed to total *internal* reflection familiar from transparent optical media. The critical angle  $\alpha_c$  of total external reflection can be derived from Snell's law, if we take into account that by convention the incident angle  $\alpha_i$  of the x-ray beam is measured relative to the substrate surface:

$$\alpha_c = (2\delta)^{1/2}$$

$\delta$  depends on the electron density of the material [2], and for typical materials we get the following values of the critical angle for 10 keV x-rays ( $\lambda = 0.124$  nm) :

organics:	$\alpha_c = 0.1$ - $0.15^\circ$
silicon and glass:	$\alpha_c = 0.18^\circ$
gold:	$\alpha_c = 0.44^\circ$

If x-rays impinge on a surface below the critical angle, they cannot propagate into the material. Instead the electric field associated with the x-ray beam is exponentially attenuated and hence scattering from the bulk is suppressed.

Working at small incident angles poses some constraints on the substrate surface quality: it should be as flat as possible and with low roughness. Polished silicon wafers with a thin oxide layer are the ideal and readily available substrate material for GISAXS. On a lower budget, glass slides work similarly well, but have a higher background. The other critical constraint of working close to the critical angle is that the line-up has to be just so: a typical substrate with 20 mm width along the beam and at  $0.2^\circ$  incident angle

exposes a cross section of only 30  $\mu\text{m}$  to the beam. In order to avoid excessive parasitic scattering the incident beam is also set to only 100  $\mu\text{m}$  or less in height. This requires a thorough line-up procedure. In addition it is very useful to collect the x-ray reflectivity in the vicinity of the critical angles as well. Due to the strong scattering in this angle range, the reflectivity can be detected with the direct beam monitor.

So why are we going to the effort of using GISAXS? The answer lies in the kind of sample we would like to study: a typical organic or inorganic film has a thickness somewhere between 30 nm to 300 nm. Due to the small incident angle we typically probe an area given by the elongated footprint of the x-ray beam on the sample. The horizontal beam width is typically around 0.5 mm, and the footprint extends the full length of the sample along the beam direction. Typical GISAXS samples are 10-30 mm in size, so we probe a macroscopic area on the surface of several  $\text{mm}^2$ , while structures have periods of 1-100 nm! Moreover, the scattering signal is proportional to the squared volume of the illuminated sample area which for a 100 nm film on a 20 mm substrate amounts to  $10^6 \mu\text{m}^3$ . In comparison a typical transmission SAXS beam probes an area of about 1 mm x 1 mm, that is a factor 10 less scattering volume and thus a factor 100 less scattering intensity. On top of this there is the attenuation by the substrate which for a 0.5 mm silicon wafer at 10 keV reduces the transmission to 3%. And we don't get information along the height of the film. So that's why we go for grazing incidence.

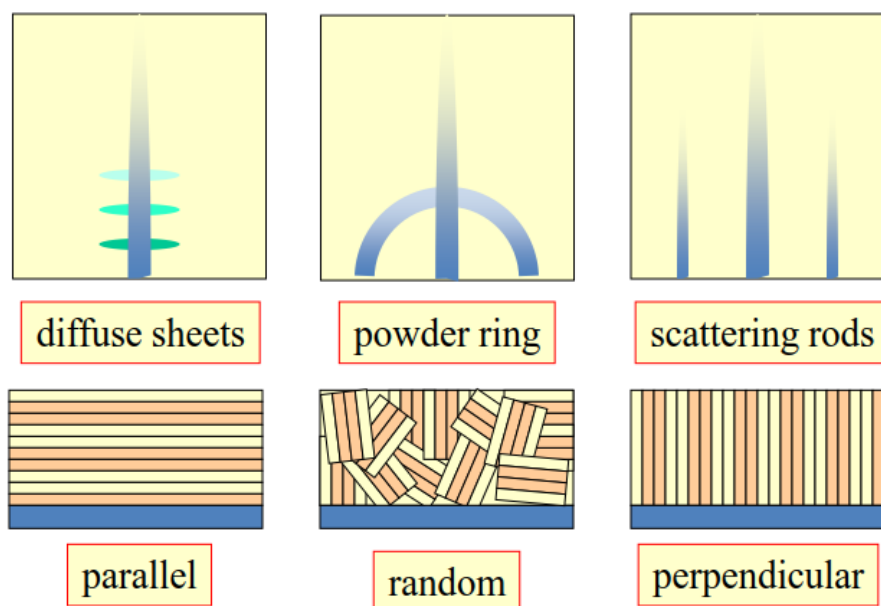


Figure 1. GISAXS signatures of parallel, random, and perpendicular lamellae (from left to right).

Figure 1 illustrates the power of GISAXS using the simplest system, regularly spaced lamellae. Lamellae are formed by a variety of soft matter systems such as block copolymers or surfactants. Lamellar stacks only produce Bragg peaks in a direction perpendicular to the lamellar planes. The scattering vector is simply given by the lamellar period  $L$ :

$$q_{lam} = \frac{2\pi}{L}$$

If lamellae are oriented parallel to the substrate, we get scattering peaks in the incident plane along the surface normal. For lamellae with random orientation we obtain a powder ring. Due to the fact that scattered x-rays are blocked by the substrate, the powder ring is only visible for exit angles larger than zero. If the lamellae are partially oriented the powder rings will become arcs. Finally for perpendicular lamellae we will observe Bragg reflections in the direction parallel to the substrate surface. Parallel and perpendicular lamellae are associated with the interaction of substrate and polymer film as well as the free surface energy of the film at the air-polymer interface [3], while rings or arcs are observed in disordered systems, such as block copolymers right after spin coating, or thick films where the interface-induced order does not persist throughout the whole film thickness.

## Basic GISAXS scattering theory

There are already some excellent introductory papers on GISAXS scattering theory [4] [5] [6]. Here we give a basic introduction that focuses on concepts rather than on the complete mathematical description. The goal is to make some peculiar scattering features of GISAXS more accessible.

As we saw in the SAXS chapter, transmission SAXS is described within the Born approximation (BA). If  $\phi_i$  and  $\phi_s$  denote the incoming and scattered plane wave, the scattering intensity is given by

$$I_{BA} \propto \left| \langle \phi_s | \rho | \phi_i \rangle \right|^2$$

where  $\rho$  is the electron density distribution of the scattering material. With  $\phi_i$  and  $\phi_s$  being plane waves, the scattering intensity is essentially the squared modulus of the Fourier transform of the electron density with respect to the scattering vector  $q$ , the difference between outgoing and incoming wave vectors of the respective waves.

In reflection geometry we have to work with the reflectivity wave functions to capture all scattering contributions. Fortunately the reflectivity wave functions are just a linear combination of the incoming and reflected waves:

$$\psi = \phi_i + r\phi_r$$

The complex reflection factor  $r$  determines the amplitude and phase of the reflected wave relative to the incident wave and is a function of the incident angle (see [7] for details). Now we are ready to write down the GISAXS scattering amplitude

$$I_{DWBA} \propto \left| \langle \psi^s | \rho | \psi^i \rangle \right|^2$$

As we have replaced the simple plane waves of the BA with the reflectivity eigenfunctions, this approximation has been termed the “distorted wave” Born approximation (DWBA). Before we evaluate this expression further, let’s take a look at the reflectivity eigenfunctions. The x-ray reflectivity  $R$  is given as

$$R = |r|^2$$

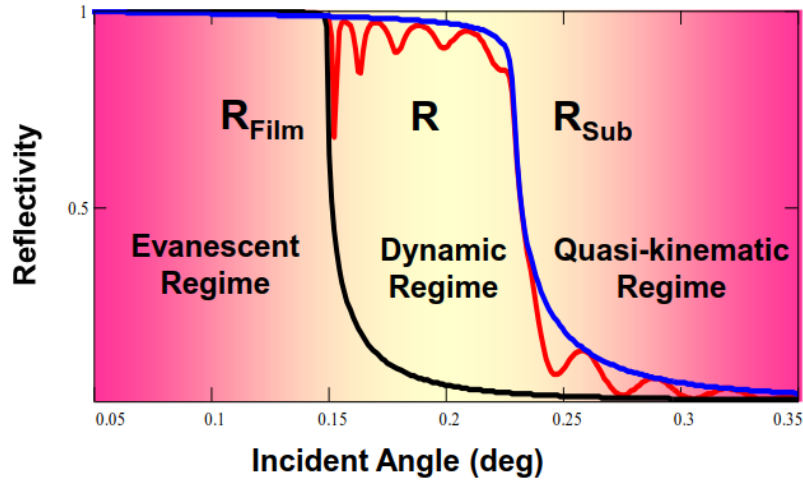


Figure 2: Typical x-ray reflectivity curves and associated GISAXS scattering regimes.

In Figure 2 typical x-ray reflectivity curves are shown – substrate (blue), film material (black), and the combined reflectivity of a thin film on a denser substrate (red). Striking features of the latter are the oscillations between the critical angles and above the critical angle of the substrate. The oscillations of the intensity above  $\alpha_{c_s}$  are the well-known Kiessig fringes [8], that are due to interference of the wave scattered from the surface and the interface of the film, and provide a precise determination of the film thickness. The oscillations between the critical angles are of a different nature. Here the reflected wave is almost as strong as the incident wave, and a standing wave field forms [9]. When a node of this wave field coincides with the film surface, a resonance condition is attained, and the wave gets trapped inside the film, similar to a waveguide [10]. Because of the wave getting trapped in the film, there is more absorption, and the waveguide modes show up at *minima* in the reflectivity curve.

Because of the strong interplay of incident and reflected wave, the scattering regime between the critical angles can be termed the *dynamic* regime, in analogy of the dynamic theory of x-ray diffraction. There are two other regimes where for the most part only one wave comes into play: In the *evanescent* regime the incident wave impinges below the critical angle of the *film* material and undergoes total external reflection. Hence the scattering intensity gets exponentially damped in the film, and at about half the critical angle the penetration depth of the wave reaches a minimum penetration of about 5-10 nm [7]. This regime is often used to obtain information about the near-surface region of the film, as compared to the fully penetrated film at higher scattering angles. Finally, beyond the critical angle of the *substrate* there is the *quasi-kinematic* regime: when the intensity of the reflected wave is below 10% of

that the incident wave, interference effects can be neglected, except for the Yoneda band of the scattered wave. In this regime scattering intensities are much lower, but the scattering theory can be much simplified [11] [12].

When we look at a typical GISAXS image of a smooth film, as shown in Figure 3, we see a system of bright horizontal lines between the critical angles of film and substrate. These are due to the standing waves/waveguide resonances in the *scattered* wave: in this case scattering from the film is enhanced and the resonance show up as *maxima*. The complex behavior between the critical angles is related to the Yoneda peak in diffuse reflectivity and the Vinyard peak in grazing incidence diffraction and originates from the incident and reflected wave being of similar amplitude and scattering in-phase [7]. Because in GISAXS we are in the vicinity of the incident plane, we have termed the bright band of scattering between the critical angles the Yoneda band. The Yoneda band is a feature of the scattered wave and thus related to the scattered wave field in the DWBA.

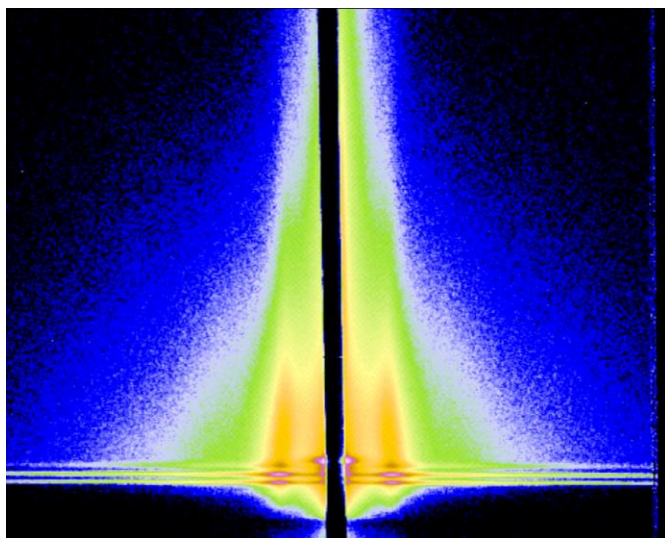


Figure 3. Yoneda band with 3 waveguide resonances, showing up as the bright lines of scattering between the critical angles. The vertical streaks are due to standing cylinders in the block copolymer thin film.

For practical purposes the first waveguide mode, just above the critical angle of the film is very useful: The wave field probes all the interior of the film, and scattering intensity is enhanced. Higher-order waveguide modes have nodes inside the film. This can be used for very precise structure determination [13] but is beyond the scope of this tutorial. In figure 4 we show the resonant scattering as the *incident* wave goes through the resonances. It needs to be emphasized that this behavior can only be observed in very flat and smooth films, such as spin-coated polymer films, so that the incident angle is well-defined.

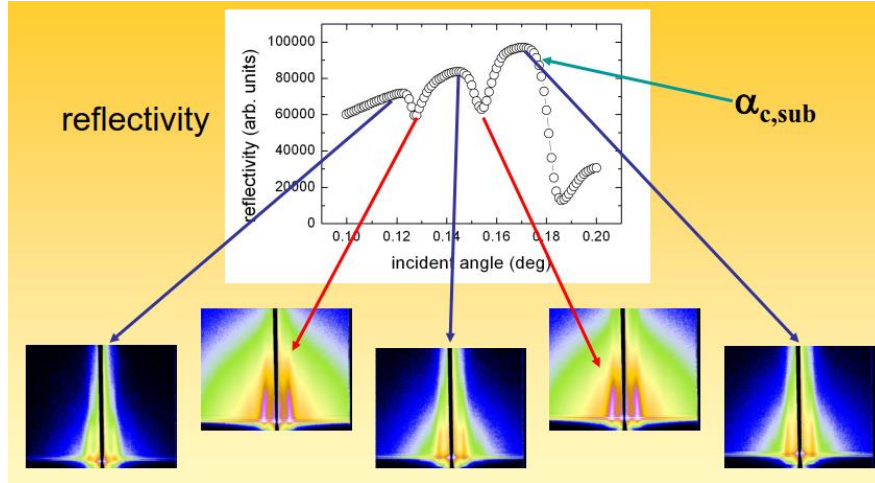


Figure 4. Reflectivity curve between the critical angles with two waveguide resonances and associated scattering images taken at the same exposure time. The intensity enhancement due to the waveguide resonances is clearly visible.

So back to the original purpose: how do we derive quantitative information about the film? First of all we note that the GISAXS intensity factors into scattering parallel to the surface and perpendicular to it. The parallel part essentially can be evaluated as SAXS in the BA. However, the scattering in the perpendicular direction turns out to be more complex. We will now evaluate the DWBA matrix element which yields:

$$I_{DWBA} \propto \left| \langle \phi_i^s | \rho | \phi_i^i \rangle + r^i \langle \phi_i^s | \rho | \phi_r^i \rangle + r^s \langle \phi_r^s | \rho | \phi_i^i \rangle + r^i r^s \langle \phi_r^s | \rho | \phi_r^i \rangle \right|^2$$

The leading term is the BA matrix element referring to the direct scattering process. The other matrix elements refer to processes where either the incoming beam gets reflected before scattering or the scattered beam gets reflected after scattering or both, respectively. As it turns out, the squared moduli of these 4 matrix elements are the dominant contribution to the scattering [6], although occasionally a mixed interference term can show similarly strong effects [5]. Terms 1 and 4 yield scattering in the same direction (the double reflections in term 4 cancel out), as do term 2 and 3 involving a single reflection. This characteristic of the scattering process produces doubled-up features in the dynamic scattering regime: there is the scattering from the direct beam and the scattering from the reflected beam.

For practical applications we distinguish 2 important cases:

- one interface, objects on the substrate surface
- thin film with 2 interfaces and embedded objects

The first case corresponds to the above equation and is important to characterize nanoscopic objects on the substrate surface. This can be for instance metal clusters on an oxide surface [4], self-organized

quantum dots [14] or a layer of nanoparticles [11]. The associated DWBA wave function is well discussed in literature [4].

The second case which is one of the most-applied scattering geometries has an extra challenge: The reflectivity wave function has now 3 regions (vacuum/film/substrate). However, the wave function remains a simple superposition of two plane waves in each region, as in the previous case. In addition it is very important to take the refraction of the x-ray beam into account. Specifically for the vertical component of the wave vector  $\kappa$  inside the film the following holds:

$$\kappa_z^i = \sqrt{(k \sin \alpha_c)^2 - (k_z^i)^2}$$

where  $\kappa_z^i$  is the wave vector component inside the medium.

If there is a scattering event inside the film with associated scattering vector  $\mathbf{q}$ , then the following holds for the z components:

$$\kappa_z^s = \kappa_z^i \pm q_z$$

The plus sign refers to the direct and double-reflected scattering events, the minus sign to the scattering events involving a single reflection [5].

Finally the scattered wave vector undergoes refraction as it leaves the film:

$$k_z^s = \sqrt{(k \sin \alpha_c)^2 + (\kappa_z^s)^2}$$

With the help of these formulae, we can relate the vacuum vector components to the scattering inside the film [5]:

$$k_z^{s\pm} = \sqrt{(k \sin \alpha_c)^2 + (\kappa_z^i \pm q_z)^2} = \sqrt{(k \sin \alpha_c)^2 + (\sqrt{(k \sin \alpha_c)^2 - (k_z^i)^2} \pm q_z)^2}$$

Thus the z-component of apparent scattering vector as measured on the detector in the air/vacuum region is related to the z-component of the scattering vector inside the material by

$$q_z^{app} = k_z^{s\pm}(q_z) - k \sin(\alpha_c)$$

Figure 5 shows a typical application of this refraction/reflection correction for the case of a block copolymer film featuring parallel lamellae. Due to the weak scattering intensities these measurements were performed in the dynamic regime for a range of incident angles. The resulting peak positions as a function of incident angle can be fitted by two parameters:  $\alpha_{cF}$ , the critical angle of the film, and the lamellar period  $L$ , which relates to the scattering vector associated with the parallel lamellae as  $q = 2\pi/L$ . Note that without taking the refraction/reflection effect into account, a naive determination of the period using the vacuum wave vectors would either yield values that are off (red branch – direct scattering) or outright wrong (green branch – reflected beam scattering).

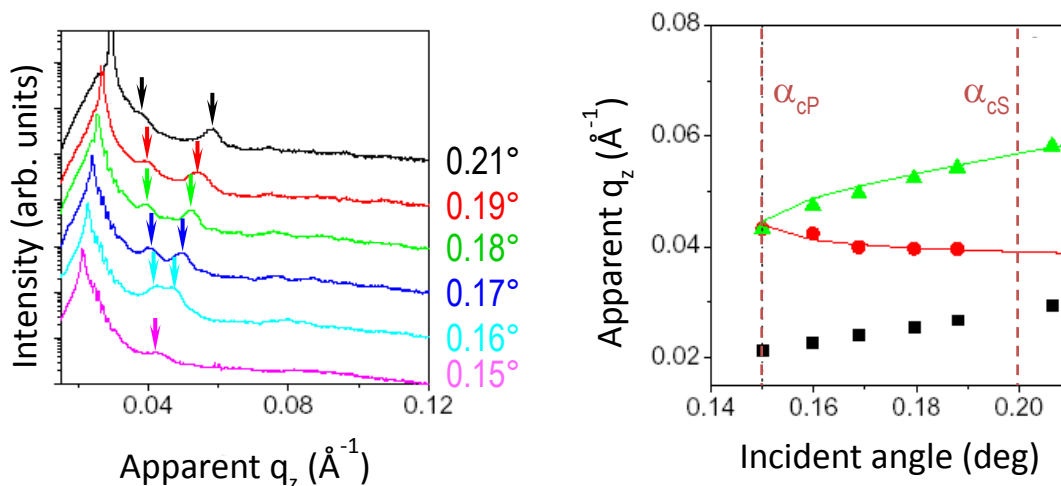


Figure 5. Vertical scattering intensity close to the beamstop of a film consisting of parallel lamellae. Left panel: The lamellar peaks show a specific shift and splitting as a function of the incident angle in the dynamic range due to the refraction/reflection effect. Right panel: Fitting the peak positions with the formula for the apparent  $q_z$  yields a polymer critical angle of  $0.15^\circ$  and a lamellar spacing of 19.7 nm.

If we have a truly 3D lattice, the refraction formulae are also to be used to model the perpendicular peak locations properly and derive the correct vertical periodicity. The case of scattering objects enclosed in a film has been discussed by a variety of authors [5] [6] [15] [16]. As a general rule we always need the scattering layer and the refracted wave vectors therein to take into account, also for more complex multilayer systems.

In the full-fledged DBWA scattering theory, the refraction correction is included automatically as a property of the reflectivity wave functions. A variety of codes are available for simulation of scattering images: e.g. IsGISAXS [4] [17], FitGISAXS [18] [19], HipGISAXS [20] [21], and BornAgain [22]. The tutorial by Müller-Buschbaum provides a step-by-step introduction to IsGISAXS, how adding features to the electron density distribution contributes to the scattering pattern [23].

### Application examples

Having delved deeply into the subtleties of the GISAXS process, the time has come to reward ourselves with some pretty pictures. When GISAXS was initially applied to thin films of soft materials, much work was done on block copolymers. All known phases of diblock copolymers have been observed by now. In addition the thin film interfaces often induce a preferential orientation of the polymer domains. Both parallel and perpendicular lamellae and cylinders have been observed. In addition BCC spheres [16], the gyroid [6] and hexagonally perforated lamellae [24] were identified. Silica mesophases [25] and nanoporous thin films [15] [26] behave quite similar to block copolymers, and display analogous structures.

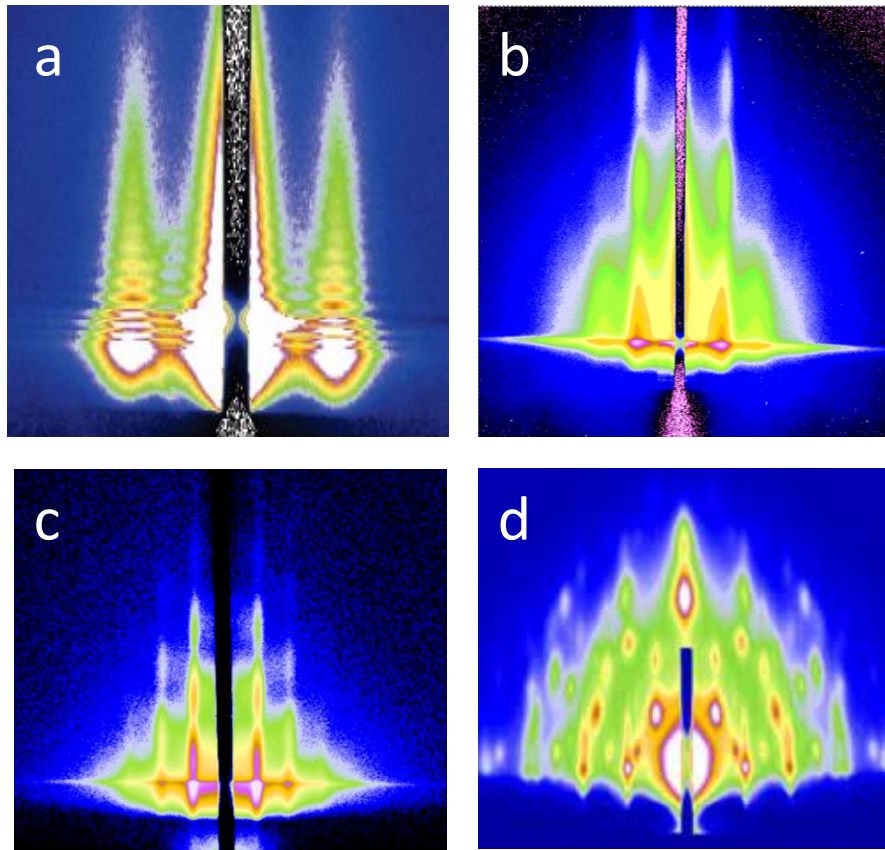


Figure 6: A glance at the variety of GISAXS images for block copolymer-derived structures: (a) standing cylinders with height corresponding to the film thickness [27] (b) monolayer of spherical voids in a silica matrix [28] (c) monolayer of shear-oriented lying cylinders [29] (d) titania gyroid after pyrolysis of the original block copolymer [26]. More detailed information about the samples can be found in the indicated literature.

Another important target material is self-assembled nanocrystal superlattices. Nanoparticles are typically synthesized in the 2-20 nm size range. In addition a variety of shapes can be obtained which have influence on the superlattice symmetry [30]. Simple round particles with short ligands form a dense FCC packing. If ligands are on the same length as the particle diameter, entropy wins out and particles form BCC packing [31], similar to the situation of blockcopolymer micelles [32]. Another case arises for non-spherical particles: nano-octahedra pack in a very open bcc packing with an unusual tip-to-tip orientation of adjacent particles [33]. A possible reason for this behavior may be the low density of ligands at corners and edges as opposed to the flat faces.

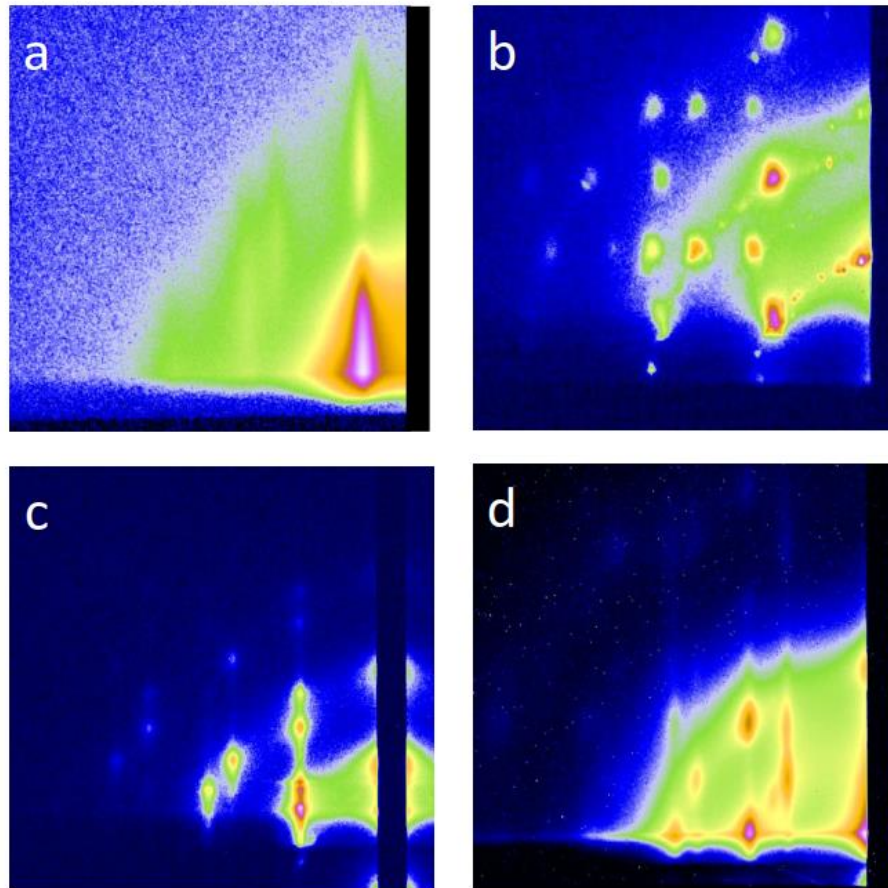


Figure 7. Overview of the variety of nanocrystal superlattices. (a) Hexagonal monolayer of FePt nanospheres [11], (b) BCC lattice of Pt<sub>3</sub>Ni nano-octahedra [33], (c) Rhombohedral arrangement of PbS nanocubes [34] (d) Binary AB<sub>2</sub> superlattice of Fe oxide and gold nanoparticles [35].

Even the crystallization of nanocubes is more complex as one would assume: simple cubic, tetragonal, and rhombohedral superlattices have been observed, depending on the specific crystallization conditions [36] [34]. Particles with pronounced non-spherical character such as nanorods [37] or platelets [38] display other types of lattices. Finally, binary superlattices consisting of two particles of different size form yet another sequence of lattice morphologies [35] [39].

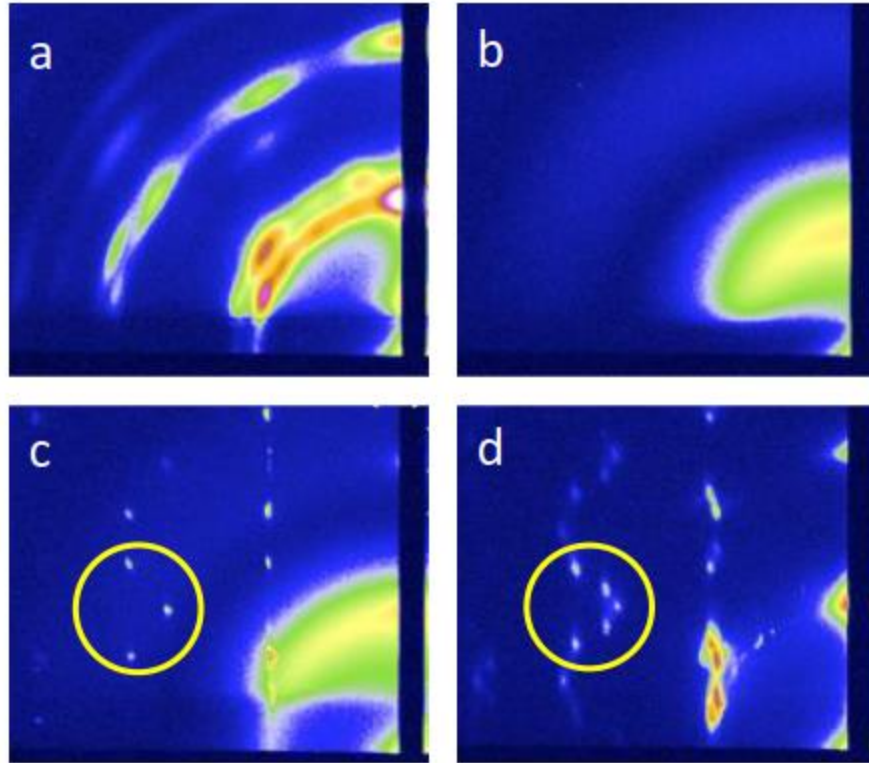


Figure 8. Lead sulfide nanocrystal superlattices: (a) after dropcasting a 3D FCC lattice is formed with random orientation of the superlattice grains (b) in hexane vapor the nanocrystals return to the solution phase (c) onset of crystallization with some solvent left: a well-oriented FCC phase develops with the (111) plane parallel to the substrate. (d) Upon further drying the nanocrystals “feel” their neighbors stronger and the lattice becomes body-centered tetragonal, as evidenced by the spot splitting indicated by the yellow circles. Shrinkage in one of the  $\langle 100 \rangle$  direction is stronger than in the others. Eventually the superlattice goes through the full Bain transition and ends up BCC. For a detailed description see references [40] and [41].

A spectacular orientational transition was observed for cuboctahedral particles: as the solvent evaporates, they start out with isotropic orientation of the individual particles, the well-known Kirkwood-Alder transition for spherical colloids (Gast/Russel), but as particles get closer they start to feel the anisotropy in the ligand sphere stronger, and undergo a continuous Bain transition from FCC through a variety of tetragonal phases to finally a BCC structure (Bian, Weidner). Grazing-incidence wide-angle x-ray scattering revealed that these particles acquire more and more orientational organization as the superlattice sheds more and more interstitial solvent molecules and compacts into the bcc phase.

An overview over the variety of GISAXS applications is given in several web tutorials [1] [42] [43].

## Acknowledgements

This tutorial is the fruit of my longstanding collaborations with a number of CHESS user groups as well as discussions with other x-ray scattering experts. Specifically I would like to thank (in alphabetical order): Peter Busch, Tobias Hanrath, Andy Heitsch, Brian Korgel, Ruipeng Li, Peter Müller-Buschbaum, Ben Ocko, Christine M. Papadakis, Dorte Posselt, and Markus Rauscher. I thank Kaifu Bian, Peter Busch, Josh Choi, Phong Du, Brian Goodfellow, Tobias Hanrath, Marleen Kamperman, Christine Papadakis, Vincent Pelletier, Danielle Smith, Ben Trembl, and Jun Zhang for providing me with data files that were used in the figures. GISAXS images were plotted using the Fit2D software [44].

## References

- [1] D.-M. Smilgies, <https://www.classe.cornell.edu/~dms79/gisaxs/GISAXS.html>.
- [2] Center for X-ray Optics - CXRO, [http://henke.lbl.gov/optical\\_constants/](http://henke.lbl.gov/optical_constants/).
- [3] P. Busch, D. Posselt, D.-M. Smilgies, M. Rauscher and C. M. Papadakis, "The Inner Structure of Thin Films of Lamellar Poly(Styrene-*b*-Butadiene) Diblock Copolymers as Revealed by Grazing-Incidence Small-Angle Scattering," *Macromolecules*, vol. 40, pp. 630-640, 2007.
- [4] R. Lazzari, "IsGISAXS: a program for grazing-incidence small-angle X-ray scattering analysis of supported islands," *J. Appl. Cryst.*, vol. 35, pp. 406-421, 2002.
- [5] P. Busch, M. Rauscher, D.-M. Smilgies, D. Posselt and C. M. Papadakis, "Grazing-incidence small-angle x-ray scattering (GISAXS) as a tool for the investigation of thin nanostructured block copolymer films - The scattering cross-section in the distorted wave Born approximation," *J. Appl. Cryst.*, vol. 39, pp. 433-442, 2006.
- [6] B. Lee, I. Park, J. Yoon, S. Park, J. Kim, K.-W. Kim, T. Chang and M. Ree, "Structural Analysis of Block Copolymer Thin Films with Grazing Incidence Small-Angle X-ray Scattering," *Macromolecules*, vol. 38, pp. 4311-4323, 2005.
- [7] J. Als-Nielsen and D. McMorrow, *Elements of Modern X-ray Physics*, Oxford: John Wiley & Sons, 2011.
- [8] H. Kiessig, "Interferenz von Röntgenstrahlen an dünnen Schichten," *Annalen der Physik*, vol. 402, pp. 769-788, 1931.

- [9] J. Wang, M. J. Bedzyk and M. Caffrey, "Resonance-Enhanced X-rays in Thin Film: A Structure Probe for Membranes and Surface Layers," *Science*, vol. 258, pp. 775-778, 1992.
- [10] Y. P. Feng, S. K. Sinha, H. W. Deckman, J. B. Hastings and D. P. Siddons, "X-Ray Flux Enhancement in Thin-Film Waveguides Using Resonant Beam Couplers," *Phys. Rev. Lett.*, vol. 71, pp. 537-540, 1993.
- [11] A. T. Heitsch, R. N. Patel, B. W. Goodfellow, D.-M. Smilgies and B. A. Korgel, "GISAXS Characterization of Order in Hexagonal Monolayers of FePt Nanocrystals," *J. Phys. Chem. C*, vol. 114, p. 14427–14432, 2010.
- [12] D.-M. Smilgies, A. T. Heitsch and B. A. Korgel, "Stacking of Hexagonal Nanocrystal Layers during Langmuir–Blodgett Deposition," *J. Phys. Chem. B*, vol. 116, p. 6017–6026, 2012.
- [13] Z. Jiang, D. R. Lee, S. Narayanan and J. Wang, "Waveguide-enhanced grazing-incidence small-angle x-ray scattering of buried nanostructures in thin films," *Phys. Rev. B*, vol. 84, p. 075440, 2011.
- [14] T. H. Metzger, I. Kegel, R. Paniago, A. Lorke, J. Peisl, J. Schulze, I. Eisele, P. Schittenhelm and G. Abstreiter, "Shape, size, strain and correlations in quantum dot systems studied by grazing incidence X-ray scattering methods," *Thin Solid Films*, vol. 336, pp. 1-8, 1998.
- [15] M. P. Tate, V. N. Urade, J. D. Kowalski, T.-C. Wei, B. D. Hamilton, B. W. Eggiman and H. W. Hillhouse, "Simulation and Interpretation of 2D Diffraction Patterns from Self-Assembled Nanostructured Films at Arbitrary Angles of Incidence: From Grazing Incidence (Above the Critical Angle) to Transmission Perpendicular to the Substrate," *J. Phys. Chem. B*, vol. 110, pp. 9882-9892, 2006.
- [16] G. E. Stein, E. J. Kramer, X. Li and J. Wang, "Layering Transitions in Thin Films of Spherical-Domain Block Copolymers," *Macromolecules*, vol. 40, pp. 2453-2460, 2007.
- [17] R. Lazzari, <http://ln-www.insp.upmc.fr/oxydes/IsGISAXS/isgisaxs.htm>.
- [18] D. Babonneau, "FitGISAXS: software package for modelling and analysis of GISAXS data using IGOR Pro," *J. Appl. Cryst.*, vol. 43, p. 929–936, 2010.
- [19] Babonneau, <https://www.pprime.fr/?q=fr/nanoparticules-nanostructures>.
- [20] S. Chourou, A. Sarje, X. S. Li, E. Chan and A. Hexemer, "HipGISAXS: A High Performance Computing Code for Simulating Grazing Incidence X-Ray Scattering Data," *J. Appl. Cryst.*, vol. 46, pp. 1781-1795, 2013.
- [21] <https://github.com/HipGISAXS/HipGISAXS>, <https://github.com/HipGISAXS/HipGISAXS>.

- [22] J. Burle, C. Durniak, J. M. Fisher, M. Ganeva, G. Pospelov, W. Van Herck and J. Wuttke, "BornAgain - Software for simulating and fitting X-ray and neutron small-angle scattering at grazing incidence," <http://www.bornagainproject.org>, 2016.
- [23] P. Müller-Buschbaum, "A Basic Introduction to Grazing Incidence Small-Angle X-Ray Scattering," in *Applications of Synchrotron Light to Scattering and Diffraction in Materials (Springer Lecture Notes in Physics 776)*, Heidelberg, Springer, 2009, pp. 61-89.
- [24] I. Park, B. Lee, J. Ryu, K. Im, J. Yoon, M. Ree and T. Chang, "Epitaxial Phase Transition of Polystyrene-b-Polyisoprene from Hexagonally Perforated Layer to Gyroid Phase in Thin Film," *Macromolecules*, vol. 38, pp. 10532-10536, 2005.
- [25] A. Gibaud, D. Grosso, B. Smarsly, A. Baptiste, J. F. Bardeau, F. Babonneau, D. A. Doshi, Z. Chen, C. J. Brinker and C. Sanchez, "Evaporation-Controlled Self-Assembly of Silica Surfactant Mesophases," *J. Phys. Chem. B*, vol. 107, pp. 6114-6118, 2003.
- [26] E. Crossland, M. Kamperman, M. Nedelcu, C. Ducati, U. Wiesner, G. Toombes, M. Hillmyer, S. Ludwigs, U. Steiner, D.-M. Smilgies and H. Snaith, "A bicontinuous double gyroid hybrid solar cell," *Nano Lett.*, vol. 9, pp. 2807-2812, 2009.
- [27] M. Li, K. Douki, K. Goto, X. Li, C. Coenjarts, D.-M. Smilgies and C. K. Ober, "Spatially Controlled Fabrication of Nanoporous Block Copolymers," *Chem. Mater.*, vol. 16, pp. 3800-3808, 2004.
- [28] P. Du, M. Li, K. Douki, X. Li, C. B. W. Garcia, A. Jain, D.-M. Smilgies, L. J. Fetters, S. M. Gruner, U. Wiesner and C. K. Ober, "Ober Additive-driven Phase Selective Chemistry in Block Copolymer Thin Films: The Convergence of Top Down and Bottoms Up Processing," *Adv. Mater.*, vol. 16, pp. 953-957, 2004.
- [29] V. Pelletier, D.-M. Smilgies and P. Chaikin, *unpublished*.
- [30] Z. Quan and J. Fang, "Superlattices with non-spherical building blocks ( ) ,," *Nano Today*, vol. 5, p. 390—411, 2010.
- [31] Y. Yu, B. Goodfellow, M. Rasch, C. Bosoy, D.-M. Smilgies and B. A. Korgel, "The Role of Halides in the Ordered Structure Transitions of Heated Gold Nanocrystal Superlattices," *Langmuir*, vol. 31, p. 6924–6932, 2015.
- [32] G. A. McConnell, A. P. Gast, J. S. Huang and S. D. Smith, "Disorder-Order Transition in Soft Sphere Polymer Micelles," *Phys. Rev. Lett.*, vol. 71, pp. 2102-2105, 1993.

- [33] J. Zhang, Z. Luo, Z. Quan, Y. Wang, A. Kumbhar, D.-M. Smilgies and J. Fang, "Low Packing Density Self-Assembled Superstructure of Octahedral Pt<sub>3</sub>Ni Nanocrystals," *Nano Lett.*, vol. 11, p. 2912–2918, 2011.
- [34] J. J. Choi, K. Bian, W. J. Baumgartner, D.-M. Smilgies and T. Hanrath, "Interface-Induced Nucleation, Orientational Alignment and Symmetry Transformations in Nanocube Superlattices," *Nano Lett.*, vol. 12, p. 4791–4798, 2012.
- [35] D. K. Smith, B. Goodfellow, D.-M. Smilgies and B. A. Korgel, "Self-Assembled Simple Hexagonal AB<sub>2</sub> Binary Nanocrystal Superlattices: SEM, GISAXS and Substitutional Defects," *J. Am. Chem. Soc.*, vol. 131, p. 3281–3290, 2009.
- [36] S. Disch, E. Wetterskog, R. P. Hermann, G. Salazar-Alvarez, P. Busch, T. Brückel, L. Bergström and S. Kamali, "Shape Induced Symmetry in Self-Assembled Mesocrystals of Iron Oxide Nanocubes," *Nano Lett.*, vol. 11, p. 1651–1656, 2011.
- [37] C. Ocier, D.-M. Smilgies, R. Robinson and T. Hanrath, "Reconfigurable Nanorod Films: An In-Situ Study of the Relationship Between Tunable Nanorod Orientation and the Optical Properties of their Self-Assembled Thin Films," *Chem. Mater.*, vol. 27, p. 2659–2665, 2015.
- [38] A. E. Saunders, A. Ghezelbash, D.-M. Smilgies, M. B. Sigman Jr. and B. A. Korgel, "Columnar Self-Assembly of Colloidal Nanodisks," *Nano Lett.*, vol. 6, pp. 2959–2963, 2006.
- [39] B. E. Treml, B. Lukose, P. Clancy, D.-M. Smilgies and T. Hanrath, "Connecting the Particles in the Box -Controlled Fusion of Hexamer Nanocrystal Clusters within an AB<sub>6</sub> Binary Nanocrystal Superlattice," *Sci. Rep.*, vol. 4, p. 6731, 2014.
- [40] K. Bian, J. J. Choi, A. Kaushik, P. Clancy, D.-M. Smilgies and T. Hanrath, "Shape-anisotropy driven symmetry transformations in nanocrystal superlattice polymorphs," *ACS Nano*, vol. 5, p. 2815–2823, 2011.
- [41] M. C. Weidman, D.-M. Smilgies and W. C. Tisdale, "Kinetics of the self-assembly of nanocrystal superlattices measured by real-time in situ X-ray scattering," *Nature Materials*, DOI: 10.1038/NMAT4600.
- [42] A. Meyer, [www.gisaxs.de](http://www.gisaxs.de).
- [43] K. Yager, [www.gisaxs.com](http://www.gisaxs.com).
- [44] A. Hammersley, <http://www.esrf.eu/computing/scientific/FIT2D/>.